The EMBO Journal Vol. 22 No. 18 pp. 4607–4615, 2003

Structure of integrin $\alpha_5\beta_1$ in complex with fibronectin

Junichi Takagi[1,2,3,4], Konstantin Strokovich[5], Timothy A.Springer[1,6] and Thomas Walz[3,5]

[1]The Center for Blood Research, [6]Department of Pathology and [2]Department of Pediatrics, Harvard Medical School, 200 Longwood Avenue, Boston, MA 02115 and [5]Department of Cell Biology, Harvard Medical School, 240 Longwood Avenue, Boston, MA 02115, USA

[4]Present address: Institute for Protein Research, Osaka University, 3-2 Yamadaoka, Suita, Osaka 565-0871, Japan

[3]Corresponding authors
e-mail: takagi@protein.osaka-u.ac.jp or twalz@hms.harvard.edu

J.Takagi and K.Strokovich contributed equally to this work

The membrane-distal headpiece of integrins has evolved to specifically bind large extracellular protein ligands, but the molecular architecture of the resulting complexes has not been determined. We used molecular electron microscopy to determine the three-dimensional structure of the ligand-binding headpiece of integrin $\alpha_5\beta_1$ complexed with fragments of its physiological ligand fibronectin. The density map for the unliganded $\alpha_5\beta_1$ headpiece shows a 'closed' conformation similar to that seen in the $\alpha_V\beta_3$ crystal structure. By contrast, binding to fibronectin induces an 'open' conformation with a dramatic, ~80° change in the angle of the hybrid domain of the β subunit relative to its I-like domain. The fibronectin fragment binds to the interface between the β-propeller and I-like domains in the integrin headpiece through the RGD-containing module 10, but direct contact of the synergy-region-containing module 9 to integrin is not evident. This finding is corroborated by kinetic analysis of real-time binding data, which shows that the synergy site greatly enhances k_{on} but has little effect on the stability or k_{off} of the complex.

Keywords: conformational change/electron microscopy/fibronectin/integrin/single-particle analysis

Introduction

The integrin family of cell adhesion receptors comprises 24 distinct αβ heterodimers that recognize glycoprotein ligands in the extracellular matrix or on cell surfaces (Hynes, 2002). Integrins and their ligands play fundamental roles in all events that involve cell adhesion, detachment and migration, the hallmarks of multicellular organisms. Strict and dynamic control of the integrin's affinity for ligand by cellular mechanisms is of crucial importance, since ligand binding results in integrin signaling with the potential of changing the cell's fate. Aberrant interactions of integrins with their ligands have been implicated in many pathophysiological states. Therefore elucidation of the mechanisms for ligand recognition and signaling induced by ligand binding is key to the development of effective drugs against numerous disease processes including cancer metastasis, thrombosis and autoimmunity.

Many members of the integrin family, including $\alpha_5\beta_1$, $\alpha_8\beta_1$, $\alpha_{IIb}\beta_3$, $\alpha_V\beta_3$, $\alpha_V\beta_5$, $\alpha_V\beta_6$ and $\alpha_V\beta_8$, recognize an Arg–Gly–Asp (RGD) motif within their ligands. These ligands include fibronectin (Fn), fibrinogen, vitronectin, von Willebrand factor and many other large glycoproteins. Peptides containing this motif can efficiently block these integrin–ligand interactions. However, it is the residues outside the RGD motif that provide specificity as well as high affinity for each integrin–ligand pair. $\alpha_5\beta_1$ integrin and Fn form a prototypic integrin–ligand pair (Hynes and Yamada, 1982; Pierschbacher and Ruoslahti, 1984). This receptor–ligand pair is functionally very important because it mediates fibronectin fibril formation and governs extracellular matrix assembly, which is vital to cell function *in vivo* (Cukierman *et al*., 2001). The interaction between $\alpha_5\beta_1$ and Fn is fundamental for vertebrate development, since lack of $\alpha_5\beta_1$ or Fn results in early embryonic lethality (George *et al*., 1993; Yang *et al*., 1993; Goh *et al*., 1997). In addition to the RGD sequence present in Fn type III module 10, a set of residues present in Fn type III module 9 (synergy site) contribute to high-affinity recognition by $\alpha_5\beta_1$ (Obara *et al*., 1988; Aota *et al*., 1994; Mould *et al*., 1997, 2000; Redick *et al*., 2000; Altroff *et al*., 2003).

The crystal structure of the extracellular domain of $\alpha_V\beta_3$ integrin (Xiong *et al*., 2001) has established a basis to think about integrin function on the atomic level. The subsequent structure of $\alpha_V\beta_3$ in complex with a ligand-mimetic peptide (Xiong *et al*., 2002) provided a first glimpse as to how integrins recognize the RGD tripeptide motif, where Arg and Asp side chains bridge the integrin α and β subunits at the center of the ligand binding pocket. Recently, we have shown that binding to a small ligand-mimetic peptide converted the $\alpha_V\beta_3$ integrin extracellular domain from the compact 'bent' conformation seen in the crystal structure into a tall extended conformation, and that this conversion is essential for integrin activation (Takagi *et al*., 2002b). These studies utilized small peptides containing RGD; however, structural information using a protein ligand is needed in order to understand the contribution of residues outside the RGD–integrin interface to the specificity and stability of the physiological integrin–ligand complex, and to integrin conformation. Electron microscope images of integrins in complex with macromolecule ligands have previously been reported (Weisel *et al*., 1992; Du *et al*., 1993) but provide limited information due to both the flexible nature of the complex and the limitation of the rotary shadowing approach that prevents the determination of a three-dimensional (3D) reconstruction. Using a recombinant $\alpha_5\beta_1$ headpiece

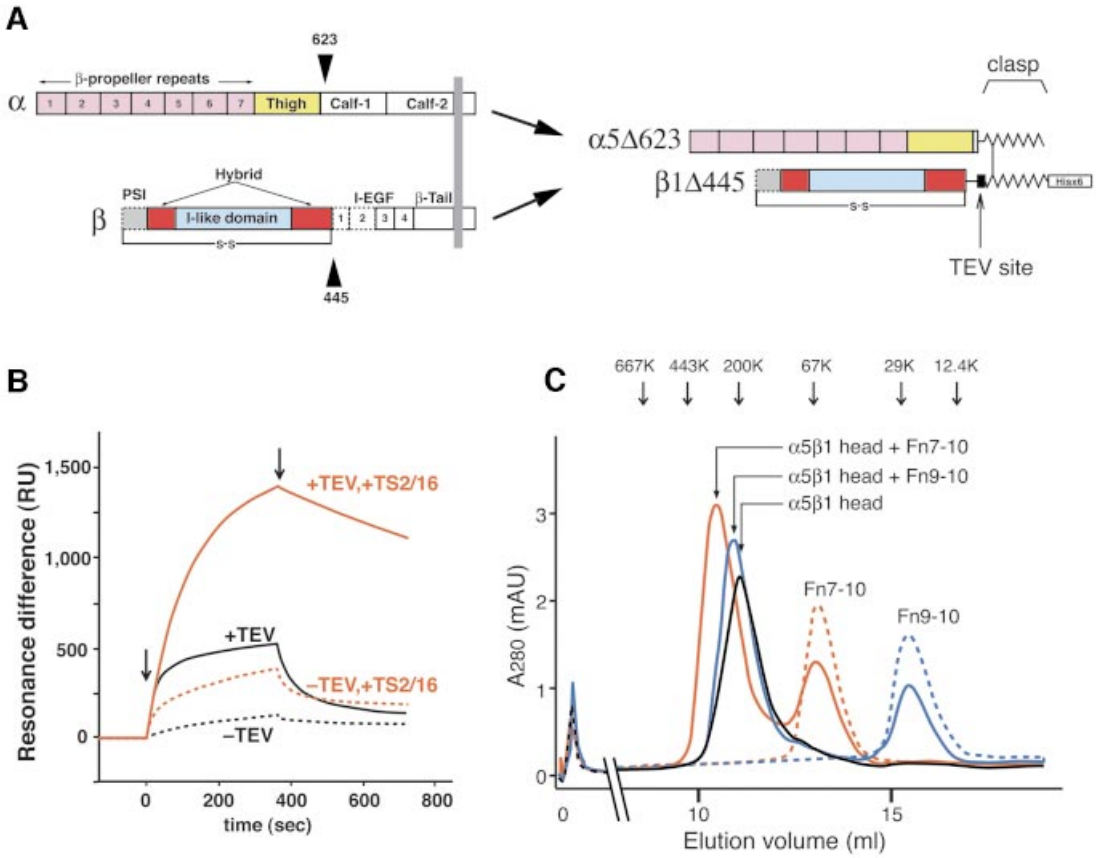

Fig. 1. The truncated $\alpha_5\beta_1$ headpiece retains its functional integrity. (**A**) The domain organization within the primary structure of integrin $\alpha_5\beta_1$ is shown on the left, and the design of the recombinant soluble $\alpha_5\beta_1$ headpiece is shown on the right. Disulfide-bonded α-helical coiled-coil domains were attached to the C-termini of the truncated subunits to act as a clasp (Takagi *et al*., 2001). Domains included in the headpiece fragment are color coded as follows: α_5 β-propeller repeat domain in pink, α_5 thigh domain in yellow, β_1 PSI domain in gray, β_1 I-like domain in cyan and β_1 hybrid domain in red. Domains not resolved in the crystal structure are depicted by dotted lines, and the position of the long-range disulfide bond present in the β subunit is shown below. (**B**) Binding analysis of Fn9–10 to the $\alpha_5\beta_1$ head fragment by surface plasmon resonance. Clasped (–TEV, dotted lines) or unclasped (+TEV, solid lines) $\alpha_5\beta_1$ headpieces were preincubated with (red lines) or without (black lines) a 3-fold molar excess of TS2/16 Fab fragment for more than 10 min and infused at a concentration of 50 nM onto the sensor surface coated with 650 RU of Fn9–10. Arrows indicate start- and end-points of the injections. (**C**) Gel filtration chromatography of the $\alpha_5\beta_1$ headpiece with bound ligands. The TEV-cleaved $\alpha_5\beta_1$ headpiece (~70 pmol) was incubated with 150 pmol of Fn9–10 (blue), Fn7–10 (red) or without ligands (black) in the presence of 1 mM Mn^{2+} for 1 h and separated on a Superdex 200 column. Chromatograms for 150 pmol Fn7–10 (red dotted) or Fn9–10 (blue dotted) alone are also shown. The elution positions of standard proteins are indicated by arrows (667 kDa, thyroglobulin; 443 kDa, apoferritin; 200 kDa, β-amylase; 67 kDa, serum albumin; 29 kDa, carbonic anhydrase; 12.4 kDa, cytochrome *c*).

fragment and Fn fragments, we present here for the first time 3D information on how an integrin globular head domain composed of both subunits binds its physiological protein ligand. Together with binding kinetics measurements, new insights emerge on the contribution of the synergy site in Fn to the binding to $\alpha_5\beta_1$ integrin.

Results

Preparation and ligand binding activity of the $\alpha_5\beta_1$ head fragment

Our previous electron microscopic studies on $\alpha_V\beta_3$ (Takagi *et al*., 2002b) showed that the integrin stalk regions are highly flexible. Lack of clear electron density in the midregion of the β subunit in the crystal structure also indicated structural flexibility in this region (Xiong *et al*., 2001). In order to reduce the resulting structural variability of the integrin extracellular segment, we truncated both α_5 and β_1 subunits to obtain an integrin fragment consisting exclusively of the ligand-binding headpiece (Figure 1A).

The α_5 subunit was truncated after the thigh domain and β_1 after the hybrid domain, thus retaining Cys444 predicted to form a long-range disulfide bridge with Cys7 (Figure 1A). Acidic/basic α-helical coiled-coil peptides containing disulfide-bridge forming Cys residues were attached to the C-terminus of the subunits to stabilize the heterodimer with a clasp (Figure 1A) (Takagi *et al*., 2001). Furthermore, a hexahistidine tag was fused to the C-terminus of the basic peptide to facilitate purification, and a TEV cleavage site was introduced before the coiled-coil domain to enable release of the C-terminal clasp. Cotransfection of these truncated subunits into CHO lec cells resulted in production and secretion of the clasped $\alpha_5\beta_1$ headpiece. A version without the clasp did not express well in transfected cells (data not shown). A similarly truncated $\alpha_5\beta_1$ protein ($\alpha_5\Delta613/\beta_1\Delta455$) has been reported (Coe *et al*., 2001), but a different C-terminal clasp was utilized in that construct.

In a buffer containing 1 mM Mn^{2+} the clasped $\alpha_5\beta_1$ headpiece bound very weakly to a fibronectin fragment containing Fn type III modules 9 and 10 (Fn9–10) (Figure 1B, black dotted sensorgram). The binding increased marginally when the $\alpha_5\beta_1$ headpiece was preincubated with a Fab fragment derived from the activating anti-β_1 mAb TS2/16 (red dotted sensorgram). In contrast, ligand binding activity increased significantly when the C-terminal clasp was released by TEV protease cleavage (black solid line), and binding became maximal in the presence of the activating TS2/16 Fab fragment (red solid line). The dissociation constant of Fn9–10 from this maximally activated $\alpha_5\beta_1$ headpiece was calculated from the sensorgrams as 1.68 ± 0.57 nM (n = 5). This value is comparable to that of recombinant soluble full-length $\alpha_5\beta_1$ (1.54 ± 0.27 nM, n = 6), indicating that the $\alpha_5\beta_1$ headpiece retained full ligand binding potential despite the absence of the tailpiece segments.

To form receptor–ligand complexes, unclasped $\alpha_5\beta_1$ headpiece at 7 μM was mixed with 15 μM Fn7–10 or Fn9–10 fragments in a buffer containing 1 mM Mn^{2+}. The complexes were sufficiently stable to be separated from free integrins and Fn fragments by gel filtration chromatography (Figure 1C). Binding between $\alpha_5\beta_1$ headpiece and Fn fragments had 1:1 stoichiometry because the use of a 2:1 molar excess of Fn fragments resulted in nearly 50% depletion of the free Fn7–10 and Fn9–10 peaks (Figure 1C). The complex peaks showed no shoulders corresponding to free integrin, and their positions were consistent with the expected molecular size increases by the binding of Fn9–10 (20 kDa) and Fn7–10 (40 kDa), respectively. Therefore it is concluded that under this condition all the integrin molecules are saturated with bound ligand.

Closed $\alpha_5\beta_1$ headpiece in the absence of ligand

We first imaged the unliganded unclasped $\alpha_5\beta_1$ headpiece by negative stain electron microscopy (EM). The majority of the projection averages (>90%) showed a very uniform conformation of the headpiece, both in Ca^{2+}-containing buffer (Figure 2A) and Mn^{2+}-containing buffer (not shown). The projection average of the $\alpha_5\beta_1$ headpiece was remarkably similar to the crystal structure of the extracellular domain of $\alpha_V\beta_3$ (Xiong *et al*., 2001). Therefore we calculated a molecular envelope of the $\alpha_V\beta_3$ headpiece at 25 Å resolution from the atomic coordinates and calculated regularly spaced projections at 2° intervals. Cross-correlation of these $\alpha_V\beta_3$ projections with the $\alpha_5\beta_1$ projection averages determined by negative stain EM indeed identified a very similar projection (Figure 3B) with a cross-correlation coefficient (CCC) of 1070. The average CCC for all projections was 870 ± 104 with the worst CCC being 726, indicating that the projection with the CCC of 1070 is indeed by far the best match with the EM projection average. The excellent correlation of the EM projection average with the X-ray structure projection enabled us to assign the densities in the EM map (Figure 3A) to individual integrin domains (Figure 3C). The globular head is asymmetric with a large density corresponding to the large β-propeller domain of the α subunit (Figure 3C, pink) and a smaller density corresponding to the I-like domain of the β subunit (Figure 3C, cyan). The α_5 thigh domain (Figure 3C, yellow) and the β_1 hybrid domain (Figure 3C, red) protrude from the longer axis of the globular head at an obtuse and an acute angle, respectively. Therefore the unliganded $\alpha_5\beta_1$ headpiece assumes a conformation we refer to as 'closed', which was previously visualized by EM of $\alpha_V\beta_3$ containing the complete extracellular domain (Takagi *et al*., 2002b). The position of the β_1 PSI domain, which is present in the $\alpha_5\beta_1$ headpiece construct but is lacking in the $\alpha_V\beta_3$ crystal structure (Figure 3C, dotted oval), can be clearly identified as an extra density present on the tip of the β tail. The very high percentage of particles in the closed conformation (>90%) confirmed that this is the most stable conformation of the unliganded $\alpha_5\beta_1$ headpiece, even in the absence of the tailpiece.

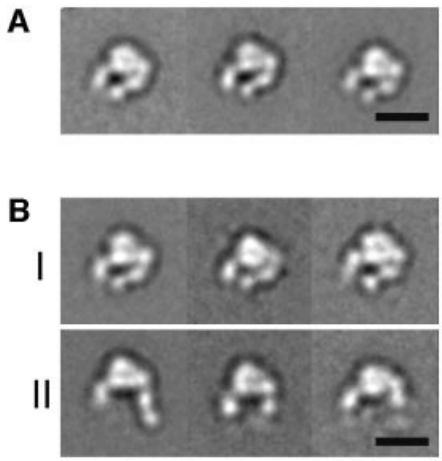

Fig. 2. Projection averages of the $\alpha_5\beta_1$ headpiece obtained by negative stain EM. The unclasped $\alpha_5\beta_1$ headpiece was incubated (**A**) without or (**B**) with 1 mM RGD peptide and imaged in the EM. In the +RGD condition, particles with closed (group I) and open (group II) conformations were observed. The three most typical averages for each group are shown, each containing 200–600 particles. Scale bars, 100 Å.

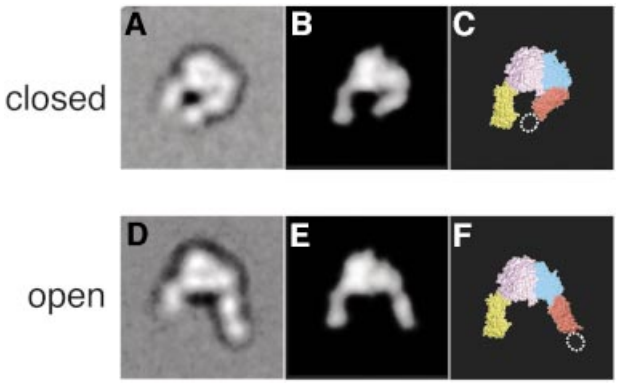

Fig. 3. Two different integrin headpiece conformations. A representative projection average from (**A**) unliganded and (**D**) liganded $\alpha_5\beta_1$ headpiece was used to identify the best-correlating projections calculated from a 25 Å density map created from $\alpha_V\beta_3$ headpiece models (**B** and **E**). The model for the open $\alpha_V\beta_3$ headpiece was prepared as described in the text and Materials and methods section. The models are shown in CPK representation (**C** and **F**) using the same color code as in Figure 1A.

RGD binding opens the $\alpha_5\beta_1$ headpiece

The same preparation of the unclasped $\alpha_5\beta_1$ headpiece was incubated with 1 mM GRGDNP peptide in 1 mM Ca^{2+}

and also imaged by negative stain EM. Although the majority of the particles still showed a closed conformation identical to that in the absence of ligand (Figure 2B, group I), about a quarter of the particles changed their shape (Figure 2B, group II). In these particles, the β hybrid domain moved away from the α_5 subunit, so that the two tails were more widely separated than in the closed conformation. In these 'open' conformations, the PSI domain was visualized in some of the averages but disappeared in others, suggesting that the hybrid–PSI connection is mobile. Conversion to the open conformation in the RGD-treated integrin headpiece is consistent with the idea that the 'hybrid domain swing' is conformationally linked to ligand binding (Takagi *et al.*, 2002b). We created a model for the $\alpha_V\beta_3$ headpiece in the open conformation (see Materials and methods). When we cross-correlated the projections from this model with the EM average (Figure 3D), we again identified a very similar projection view (Figure 3E) with a CCC of 1077, whereas the worst correlating projection yielded a CCC of 538 (with an average of 800 ± 130). It is not clear why only about a quarter of the molecules changed their shape upon RGD binding, since this peptide efficiently blocked Fn binding by full-length $\alpha_5\beta_1$ in BIAcore assays (data not shown). Complete inhibition was achieved at 1 μM ($IC_{50} \approx$ 300 nM) so that 1 mM RGD should have saturated all the binding sites. Therefore the association of linear RGDNP peptide to $\alpha_5\beta_1$ may not be sufficient to completely shift the conformational equilibrium of the headpiece fragment toward the open conformation.

Projection averages of Fn fragment and its complex with $\alpha_5\beta_1$

Despite its very small size (~40 kDa), projection averages of the negatively stained four-domain fibronectin fragment Fn7–10 showed a distinct shape with individual FnIII domains being clearly resolved (Figure 4A). The majority of the Fn7–10 fragments adopted a loosely extended conformation, but the interdomain angles seemed to be very flexible as illustrated by the presence of 'folded' particles (Figure 4A). Flexibility is consistent with the intermodule flexibility suggested by NMR studies (Copie *et al.*, 1998) and the small interfaces between individual modules in the crystal structure, which were suggested to give rise to intermodule mobility, especially at the interface between modules 9 and 10 (Leahy *et al.*, 1996). Next, we imaged a complex of the $\alpha_5\beta_1$ headpiece and the Fn7–10 fragment formed in the presence of 1 mM Mn^{2+}. About 80% of the particles had no ligand bound and showed the closed conformation identical to the one in the absence of ligands (data not shown). This is expected considering the fact that we purified the complex from the free Fn fragments and that the complex has a relatively fast dissociation rate in the absence of activating mAb (Figure 1B, black solid tracing). On the other hand, the remaining 20% had a three-legged appearance, with the C-termini of α and β chains and the Fn7–10 fragment each forming one of the three legs (Figure 4B).

The projection structures of the $\alpha_5\beta_1$ headpieces complexed with Fn7–10 provide several important insights into the ligand-recognition mechanism of $\alpha_5\beta_1$ integrin. Firstly, Fn fragment bound to the globular head at its 'top' face, which is composed of blades 2 and 3 of the

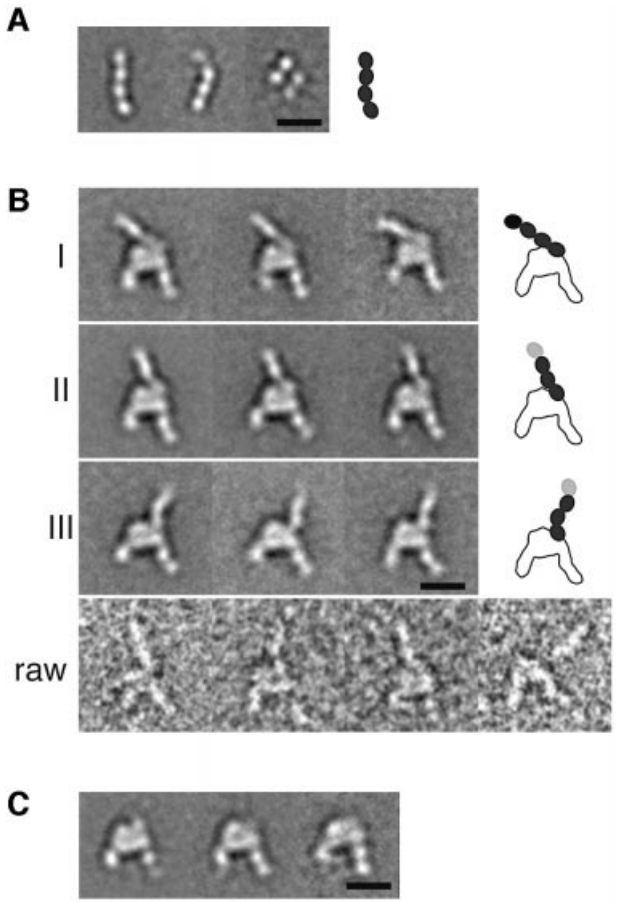

Fig. 4. $\alpha_5\beta_1$ head in complex with Fn fragment. Projection averages are shown for (**A**) Fn7–10 alone, (**B**) $\alpha_5\beta_1$ complex with Fn7–10 and (**C**) $\alpha_5\beta_1$ complex with Fn9–10. The projection averages of the $\alpha_5\beta_1$/Fn7–10 complexes are subgrouped (groups I, II and III) based on the orientation of the bound ligand, and several representative raw images are shown below (raw). As in Figure 2, the three most populated averages for each group are shown. The assignment of the FnIII modules (black ovals) in the complex is shown in the schematic drawing to the right. The modules missing in the averages due to linker flexibility are depicted by gray ovals. Scale bars, 100 Å.

α-subunit β-propeller domain and the face of the β-subunit I-like domain containing the metal-ion-dependent adhesion site (MIDAS) and a 'specificity-determining loop' (Takagi *et al.*, 2002a). Critical involvement of these segments has been suggested by many mutational and antibody mapping studies (for review see Humphries, 2000), and is now directly confirmed by our structure. Secondly, all of the $\alpha_5\beta_1$ headpieces with a bound Fn fragment assumed the open conformation, with a nearly 80° swing-out of the β tail compared with the closed conformation. This unambiguously proves that there is a direct link between ligand binding and the opening of the angle between the I-like domain and the hybrid domain. It also explains why the presence of a C-terminal clasp, which cross-links the tips of the α and β tails and thus hinders the opening of the tails, has to be removed for the $\alpha_5\beta_1$ headpiece fragment to gain full activity (Figure 1B). Thirdly, the α_5 β-propeller and the β_1 I-like domain, which together form the ligand-binding globular head, stay associated together upon ligand binding. This finding argues against the hypothesis that integrin activation/

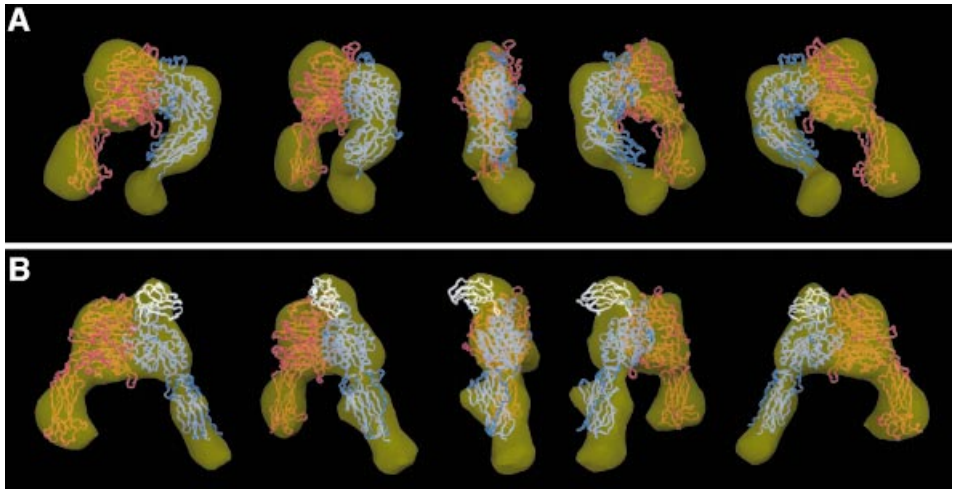

Fig. 5. Surface-rendered density maps of the $\alpha_5\beta_1$ headpiece in (**A**) the unliganded closed and (**B**) the ligand-bound open conformation. The unmodified headpiece segments of the $\alpha_V\beta_3$ crystal structure or the open $\alpha_V\beta_3$ model were manually fitted into the 3D density map of the unliganded and ligand-bound $\alpha_5\beta_1$ headpiece, respectively. Cα worm tracings for α_V, β_3 and Fn10 segments are colored in red, blue and white, respectively. Views are successive 45° rotations about the vertical figure axis. The figure was generated using DINO (Philippsen, 2002).

ligand binding is accompanied by a substantial separation of the headpieces of the two subunits (Hantgan *et al*., 1999; Liddington and Ginsberg, 2002). Lastly and most importantly, the binding of the Fn7–10 fragment to the integrin headpiece was restricted to a single contact point at the end of the Fn7–10 fragment. The remaining segments of the molecule showed no defined orientation with respect to the integrin headpiece and radiated out from it in many different directions (Figure 4B, compare groups I, II and III). Because of flexibility between adjacent FnIII modules, the most distal FnIII module tended to be averaged out in our projection averages. However, this module was present in the raw images (Figure 4B, raw), indicating that the Fn module in contact with the integrin was the 10th. This allowed us to assign the positions of the four modules in the averages using the size of a single Fn module as a guide (Figure 4A and B, right). The contact site of Fn module 10 with the integrin headpiece is located at the α/β interface, slightly shifted toward the I-like domain of the β subunit. The adjacent FnIII module 9 is positioned very close to the α_5 subunit, but in most averages the two protein domains do not seem to make contact. Group I in Figure 4B, representing ~28% of the $\alpha_5\beta_1$-Fn7–10 complexes, appears to have a relatively large contact area, which may include interactions of FnIII module 9 with the integrin headpiece. However, in groups II and III, representing 58% and 14% of the complexes, respectively, only FnIII module 10 appears to interact with the integrin headpiece.

When a two-domain fragment of fibronectin (Fn9–10) was used to form a complex with the $\alpha_5\beta_1$ headpiece, we could only see density corresponding to FnIII module 10 in the resulting averages (Figure 4C; compare with Figure 2B, group II). The adjacent module 9 was averaged out most likely due to a combined effect of its small size (compared with the remainder of the molecule) and the flexibility between modules 9 and 10. The disappearance of module 9 in the projection averages corroborates the lack of a strong interaction between the synergy site in module 9 and the integrin headpiece. All the particles that had the extra density corresponding to the bound ligand assumed the open conformation, indicating that the two-domain Fn9–10 fragment had the same effect on the integrin conformation as the four-domain Fn7–10 fragment.

Three-dimensional reconstruction

We used the random conical tilt approach (Radermacher *et al*., 1987) to calculate a 3D reconstruction of the negatively stained $\alpha_5\beta_1$ headpiece and its complex with Fn9–10 (Figure 5A and B). With a size of 170 kDa, the integrin headpiece is among the smallest molecules so far for which a structure has been determined by single-particle EM.

The resulting density map of the unliganded headpiece revealed all the expected integrin domains and allowed for a good fit with the segment of the $\alpha_V\beta_3$ crystal structure that corresponds to the headpiece (Figure 5A). However, the molecular envelope determined by EM for the unliganded $\alpha_5\beta_1$ headpiece appears to have a slightly wider opening angle between the α_5 thigh domain and the β_1 hybrid domain than in the $\alpha_V\beta_3$ crystal structure. This might be due to structural differences between the two integrins or it may reflect a slightly more relaxed conformation of the closed integrin headpiece conformation in the absence of crystal packing constraints. The extra density at the tip of the β tail in our 3D map corresponds well to the expected location of the PSI domain, which is present in our $\alpha_5\beta_1$ headpiece but is absent in the $\alpha_V\beta_3$ crystal structure.

In the 3D map of the $\alpha_5\beta_1$ headpiece in complex with Fn9–10, the orientation of the β subunit hybrid and PSI domains was very different compared with the unliganded headpiece (Figure 5B). To adjust the atomic model of the closed $\alpha_V\beta_3$ headpiece to our EM map of the liganded headpiece, the hybrid domain had to be rotated as a rigid body away from the remainder of the molecule by an angle of about 80°. The resulting model for the open conformation of the $\alpha_V\beta_3$ headpiece fits very well into the 3D map

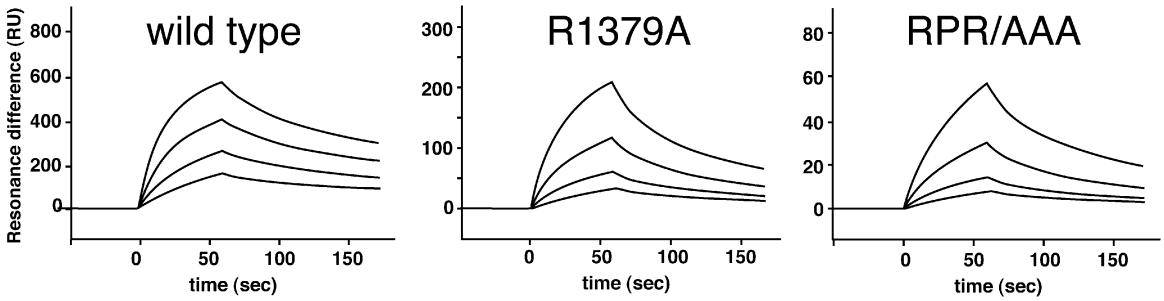

Fig. 6. Comparison of the kinetics of $\alpha_5\beta_1$ binding to recombinant Fn7–10 fragment. Either wild-type, R1379A or RPR/AAA synergy mutant Fn7–10 fragments were immobilized on the sensor chip at the same density (500 RU), and full-length $\alpha_5\beta_1$ was injected at 20 μl/min. Traces show increasing concentrations (7.5, 15, 30 and 60 nM) of $\alpha_5\beta_1$ analyte.

(Figure 5B), with the exception of an extra density at the top of the $\alpha_5\beta_1$ headpiece that represented the bound ligand. The size of this extra density was sufficient to accommodate an FnIII module, consistent with our fit of the Fn10 module to this position (Figure 5B, white Cα tracing). The oblong Fn10 module was docked into the extra density present in the $\alpha_5\beta_1$-Fn9–10 complex using the C- to N-terminal orientation derived from the images of the bound Fn7–10 fragment. In this docking model the expected ligand-coordinating metal in the β subunit's MIDAS motif is about 10 Å away from the Asp residue in the RGD loop. Given the ~25 Å resolution of our EM map and the flexibility of the RGD loop seen in NMR structures, revealing a pairwise RMS deviation of 7 Å for the side-chain Oδ atoms of the Asp (Copie *et al.*, 1998), our fit is compatible with direct coordination of the oxygen in the Asp side chain to the metal ion in the MIDAS motif.

The synergy site in FnIII module 9 has been hypothesized to be a secondary interaction site for $\alpha_5\beta_1$, directly binding to the β-propeller domain of the α_5 subunit (Mould *et al.*, 1997; Redick *et al.*, 2000). This hypothesis was based on the observations that a mutant Fn fragment lacking an intact synergy site showed greatly reduced affinity to $\alpha_5\beta_1$ compared with the wild-type fragment. However, a great reduction of total affinity does not necessarily imply a direct involvement of the mutated residue in the binding interface. The lack of an obvious interaction between the FnIII module 9 and the $\alpha_5\beta_1$ headpiece in our projection and 3D maps led us to reconsider the two-site hypothesis.

Kinetic analysis of $\alpha_5\beta_1$ binding to both wild-type and mutant Fn7–10

To determine the effect of the synergy site mutation on the kinetic behavior of Fn binding to $\alpha_5\beta_1$, we performed real-time surface plasmon resonance binding assays. Wild-type and two different synergy site mutant Fn7–10 fragments were immobilized at the same density on a sensorchip via C-terminally tagged biotin (Takagi *et al.*, 2001). One mutant (R1379A) has a single Ala mutation in the synergy site and shows mildly reduced cell adhesion activity, whereas the other mutant (R1374A/P1376A/R1379A, abbreviated as RPR/AAA) has two more Ala mutations that abolished the synergy effect of the ninth repeat on the adhesion activity (Redick *et al.*, 2000). Binding of injected soluble $\alpha_5\beta_1$ was monitored in the presence of 1 mM Mn^{2+}. Comparison of the concentration-dependent binding of wild-type and mutant ligands revealed an 11- and 45-fold decrease in the affinity of the R1379A and RPR/AAA mutants, respectively (Figure 6 and Table I). However, when we calculated the kinetic parameters for the binding, it became clear that the mutation primarily affected the association phase (5- and 26-fold decrease of k_{on} for R1379A and RPR/AAA, respectively), whereas the dissociation phase was only slightly affected (~2-fold increase in k_{off} for both mutants). In general, mutations in residues that are part of protein–protein interfaces affect mostly the dissociation rate with minimal effects on the association rate (Cunningham and Wells, 1993; Clackson *et al.*, 1998; Wu *et al.*, 2002). The reason for this is that the association phase in most protein–protein interactions is diffusion controlled (Northrup and Erickson, 1992) and, analogous to the protein-folding process (Fersht, 1997), there are many pathways that lead to an initial encounter between two components. The loss of Arg1379 cost only 0.4 kcal/mol for the stability of the complex while decreasing the rate of complex formation by a factor of 5 (0.96 kcal/mol). Moreover, the additional loss of Pro1376 and Arg1374 had no effect on the stability of the complex but resulted in an additional 5-fold reduction in the association rate. This strongly suggests that the synergy site exerts its positive effect on $\alpha_5\beta_1$ binding by facilitating the initial encounter, rather than by contributing to the protein–protein interaction surface.

Table I. Kinetic parameters for $\alpha_5\beta_1$ binding to various Fn7–10 fragments

Fn7–10 ligand	k_{on} ($\times 10^5$ M^{-1} s^{-1})	k_{off} ($\times 10^{-3}$ s^{-1})	K_D (nM)
Wild type	14.9 ± 4.9	6.5 ± 0.1	4.4
R1379A	2.8 ± 0.8	14.0 ± 1.4	50
RPR/AAA	0.58 ± 0.16	11.3 ± 2.0	195

Surface plasmon resonance binding was performed as described in Materials and methods and the kinetic parameters were derived from the sensorgrams shown in Figure 6. Values are mean ± SE obtained from four different concentrations.

Discussion

Here, a 3D reconstruction by single-particle EM yields the first 3D picture of a heterodimeric integrin headpiece in

complex with a physiological protein ligand. Visualization of the protein ligand bound to the 'top' face of the integrin headpiece confirms the location of the ligand-binding site suggested by many structural, mutational and antibody mapping studies. The large conformational change associated with ligand binding unambiguously establishes the central role of the hybrid/I-like domain angle change in affinity regulation. The magnitude of the interdomain conformational change seen here is extraordinary; the hybrid domain swings out by about 80° and moves the tip of the PSI domain some 70 Å away from the α subunit.

A resting integrin on the cell surface assumes a bent conformation unfavorable for the recognition and binding of large macromolecular ligands (Takagi *et al*., 2002b). When integrins are activated by either cellular activation mechanisms or artificial extracellular reagents, a straightening of the receptor molecule is observed (Takagi and Springer, 2002). However, the global unbending of the receptor *per se* is not likely to be responsible for the increased affinity, since the release of a C-terminal clasp (and hence the acquisition of freedom of the hybrid domain to swing) in the headpiece fragment used here increases ligand affinity even in the complete absence of a tailpiece. Therefore the swing of the hybrid domain must directly affect the conformation of the ligand-binding site on the top of the molecule. However, in the context of a full-length integrin, the same movement would also induce the straightening of the bent receptor via disruption of headpiece–tailpiece interactions. Thus the hybrid domain acts as a mechanical device that couples the conformational state of the ligand-binding site to the overall conformation of the receptor. For cell surface integrins, acquisition of high affinity by a local conformational change and better ligand accessibility by receptor extension may both be important to ensure efficient cell adhesion.

Our EM observations and kinetic measurements of the $\alpha_5\beta_1$–Fn interactions do not support the two-site binding model, which proposes that the RGD loop and the synergy site latch simultaneously onto widely separated binding pockets on the β_1 and α_5 subunits, respectively. Instead, our findings suggest that FnIII module 9 supports integrin binding in an indirect fashion, although its contribution to the overall affinity is substantial. Recent studies showed that the synergistic activity of FnIII module 9 correlates with its effect on the stability of the Fn9–10 fragment (Grant *et al*., 1997; Altroff *et al*., 2001, 2003). In one study it was shown that the mutation of a residue located on the opposite face from the synergy site in Fn9, and hence not able to contribute directly to integrin binding, canceled the deleterious effect of a synergy site mutation (Altroff *et al*., 2003). Since the Fn9–Fn10 intermodule linkage and the RGD loop are highly flexible in solution (Baron *et al*., 1992; Copie *et al*., 1998), the role of the synergy region in module 9 may therefore lie in orienting the RGD loop in a way that leads to optimal exposure of the RGD sequence for binding to an integrin receptor.

Another possible explanation for the synergy effect of module 9 is long-range electrostatic steering. A model of the $\alpha_5\beta_1$ integrin headpiece created on the basis of the crystal structure of $\alpha_V\beta_3$ revealed that there is an extensive stretch of acidic surface on the top of the α/β interface, where the ligand-binding site is located. Aside from Asp1495, which is part of the RGD sequence, the Fn9–10 segment contains several conserved acidic residues in the vicinity of the RGD loop. The association rate of wild-type Fn7–10 to $\alpha_5\beta_1$ falls in the range that is typical for diffusion-limited interactions between proteins ($0.5–5 \times 10^6$ $M^{-1}s^{-1}$) (Northrup and Erickson, 1992), whereas those of the synergy site mutants are below this range. Taken together, these observations suggest that the association of mutant Fn7–10 to $\alpha_5\beta_1$ is hampered by electrostatic repulsion, which is neutralized by basic residues contributed by the synergy site in wild-type Fn7–10. The additive effect of R1374A and R1379A mutations on the k_{off} of Fn7–10 supports this idea. Further support for this hypothesis is provided by the finding that mutating basic residues outside the classical synergy region also severely perturbed integrin binding (Redick *et al*., 2000). Structural and mutational studies on protein recognition have shown that residues outside the interaction site can make an important contribution to affinity by affecting the on-rate (Clackson and Wells, 1995). Our studies suggest that the synergy site may contribute in an analogous manner, although we cannot completely rule out a direct interaction. It is likely that the synergy site mediates transient and weak long-range interactions between Fn and the α_5 subunit that do not result in a tight association that can persist during the adsorption/staining procedure of EM sample preparation. Determination of a high-resolution crystal structure of an $\alpha_5\beta_1$–Fn complex would help to resolve the remaining ambiguities concerning the contribution of individual domains/residues in complex formation.

A series of studies have shown that residues in the α_5 subunit contribute directly to the binding of Fn (Mould *et al*., 1997; Humphries *et al*., 2000). Our EM structures are consistent with these studies, because module 10 interacts with the interface between the α and the β subunit. Some of the residues recognized by anti-α_5 blocking mAb seem to be located outside the α/β interface (Burrows *et al*., 1999), but the binding of a large IgG molecule may occlude Fn approach, especially if module 10 has an N-terminal extension (i.e. module 9).

The present study unequivocally establishes that hybrid domain swing-out is directly linked with ligand binding. Since the I-like domain is connected through both its N- and C-termini to the hybrid domain, widening of the angle between the I-like and hybrid domains is predicted to be tightly linked to a downward displacement of the C-terminal α-helix of the I-like domain, based on the overall topology of the interdomain connections (Takagi and Springer, 2002). Ligand docking and the subsequent direct coordination of an acidic residue in the ligand (e.g. Asp^{1495} of the RGD motif of fibronectin) to the MIDAS metal ion would induce this helix movement via a rearrangement of MIDAS coordinating residues, analogous to the shape-shifting pathway in α I domains (Shimaoka *et al*., 2003). Hybrid domain swing-out at the headpiece induced by ligand binding would in turn trigger a global conformational change and ultimately change the conformation of the cytoplasmic tails that link integrins to the cytoskeleton, leading to cellular signaling. Therefore in our study we have captured the first step of the integrin outside-in signaling pathway.

Materials and methods

Production of soluble recombinant $\beta_5\beta_1$ headpiece

Soluble truncated α_5 ($\alpha_5\Delta$623-AHCys) and β_1 ($\beta_1\Delta$445-tev-BHCys) constructs were prepared from wild-type human α_5 and β_1 cDNAs by overlap extension PCR using the same design as for soluble clasped $\alpha_5\beta_1$ (Takagi *et al*., 2001), except that a hexahistidine tag was fused to the C-terminus of β_1. The soluble integrin headpiece was purified from culture supernatant of stably transfected CHO lec 3.2.8.1 cells as described previously, and stored at 1–2 mg/ml in TBS (50 mM Tris–HCl pH 7.5, 150 mM NaCl) containing 1 mM $CaCl_2$ and 1 mM $MgCl_2$ at 4°C. Release of the C-terminal clasp was achieved by incubation with 250 U/ml TEV protease (Invitrogen) at 25°C for 16 h. Complete cleavage was confirmed by the conversion of the single ~150 kDa band (corresponding to the covalent dimer) to an 85 and a 55 kDa band (corresponding to truncated α_5 and β_1 monomer, respectively) on non-reducing SDS–PAGE. Unclasped $\alpha_5\beta_1$, or its complex with ligand, was purified on a Superdex 200 HR column and the peak fraction was kept on ice for less than 30 min before the preparation of EM samples.

Preparation of Fn fragments

Recombinant FnIII fragments were produced using a bacterial expression system as described previously (Takagi *et al*., 2001). Wild-type, R1379A or R1374A/P1376A/R1379A (RPR/AAA) versions of the Fn7–10 construct (gifts from Harold P.Erickson) (Redick *et al*., 2000) were modified to contain a C-terminal cysteine, which was used for the biotinylation and subsequent immobilization onto streptavidin-sensor chips (Takagi *et al*., 2001). Fn7–10 and Fn9–10 with unmodified C-termini were prepared as described (Leahy *et al*., 1994).

Electron microscopy and image processing

Samples were adsorbed to glow-discharged carbon-coated copper grids, washed with two drops of deionized water and stained with two drops of freshly prepared 0.75% uranyl formate. Grids were inspected with a Philips Tecnai 12 electron microscope operated at 120 kV, and images were recorded at a nominal magnification of 52 000× using low-dose procedures. Images were digitized with a Zeiss SCAI scanner using a step size of 7 μm and 3 × 3 pixels were averaged to yield a final pixel size of 4 Å at the specimen level. The SPIDER image processing package (Frank *et al*., 1996) was used for particle selection and for all image processing steps. For the $\alpha_5\beta_1$ headpiece in Ca^{2+} 9179 particles were selected from 26 micrographs, and for the headpiece in complex with the RGD peptide 8872 particles were selected from 42 micrographs. For the headpiece in complex with the Fn7–10 fragment we only selected particles which clearly had a ligand bound (4292 particles from 69 images). In all cases particles were classified and grouped into 50 classes using the multireference alignment procedure, and the particles in each class were averaged to produce class averages. The model for the open $\alpha_V\beta_3$ headpiece was created using the corresponding segment of the liganded $\alpha_V\beta_3$ (1LG5) (Xiong *et al*., 2002) by rotating the hybrid domain as a rigid body away from the remainder of the molecule by an angle of about 80°. For comparison with the crystal structures of $\alpha_V\beta_3$, the models were resolution filtered to 25 Å and projections calculated at an angular interval of 2° were cross-correlated with selected class averages. The reprojections with the highest correlation coefficient are shown in Figure 3B and E. The 3D reconstructions of the unliganded and the Fn9–10-liganded headpiece were calculated using the random conical tilt approach. Then, 9555 particle pairs were selected from 25 pairs of 60° and 0° tilted images. The particles selected from the untilted images were classified into 10 groups, and the largest classes representing the unliganded headpiece (2672 particles) and the Fn9–10-liganded headpiece (1005 particles) were used to calculate 3D reconstructions. The corresponding particles from the tilted images were used to calculate an initial 3D map using weighted backprojection (Radermacher, 1992). The model was refined by iterative projection matching of the original images with reprojections from the 3D map at increasingly finer angular intervals. Finally, 500 untilted images for the unliganded headpiece and 1300 images for the Fn9–10-liganded headpiece were included in the dataset. Fourier shell correlation (FSC) using the FSC > 0.5 criterion indicated a resolution of 20 Å for the unliganded headpiece and 24 Å for the Fn9–10-liganded headpiece. The density maps shown in Figure 3 were both resolution filtered to 24 Å.

Surface plasmon resonance

Experiments were done using the BIAcore 3000 (Biacore AB). Dilutions of $\alpha_5\beta_1$ headpiece fragment (clasped or unclasped) in TBS containing 1 mM $MnCl_2$ were injected at 20 μl/min into flow cells containing 500–800 RU of Fn fragment. All measurements were baseline corrected by subtracting the sensorgram obtained with control streptavidin surface and kinetic parameters were determined by fitting the data to a 1:1 Langmuir binding model using BIAevaluation software ver3.0.

Acknowledgements

We thank H.P.Erickson for providing the mutant Fn constructs. This work was supported by NIH grant HL48675 (to T.A.S. and J.T.). The molecular EM facility at Harvard Medical School was established by a generous donation from the Giovanni Armenise Harvard Center for Structural Biology and is maintained by funds from NIH grant GM62580.

References

Altroff,H., van Der Walle,C.F., Asselin,J., Fairless,R., Campbell,I.D. and Mardon,H.J. (2001) The eighth FIII domain of human fibronectin promotes integrin $\alpha_5\beta_1$ binding via stabilization of the ninth FIII domain. *J. Biol. Chem.*, **276**, 38885–38892.

Altroff,H., Choulier,L. and Mardon,H.J. (2003) Synergistic activity of the ninth and tenth FIII domains of human fibronectin depends upon structural stability. *J. Biol. Chem.*, **278**, 491–497.

Aota,S., Nomizu,M. and Yamada,K.M. (1994) The short amino acid sequence Pro–His–Ser–Arg–Asn in human fibronectin enhances cell-adhesive function. *J. Biol. Chem.*, **269**, 24756–24761.

Baron,M., Main,A.L., Driscoll,P.C., Mardon,H.J., Boyd,J. and Campbell,I.D. (1992) 1H NMR assignment and secondary structure of the cell adhesion type III module of fibronectin. *Biochemistry*, **31**, 2068–2073.

Burrows,L., Clark,K., Mould,A.P. and Humphries,M.J. (1999) Fine mapping of inhibitory anti-α 5 monoclonal antibody epitopes that differentially affect integrin–ligand binding. *Biochem. J.*, **344**, 527–533.

Clackson,T. and Wells,J.A. (1995) A hot spot of binding energy in a hormone-receptor interface *Science*, **267**, 383–386.

Clackson,T., Ultsch,M.H., Wells,J.A. and de Vos,A.M. (1998) Structural and functional analysis of the 1:1 growth hormone:receptor complex reveals the molecular basis for receptor affinity. *J. Mol. Biol.*, **277**, 1111–1128.

Coe,A.P., Askari,J.A., Kline,A.D., Robinson,M.K., Kirby,H., Stephens,P.E. and Humphries,M.J. (2001) Generation of a minimal $\alpha_5\beta_1$ integrin-Fc fragment. *J. Biol. Chem.*, **276**, 35854–35866.

Copie,V., Tomita,Y., Akiyama,S.K., Aota,S., Yamada,K.M., Venable,R.M., Pastor,R.W., Krueger,S. and Torchia,D.A. (1998) Solution structure and dynamics of linked cell attachment modules of mouse fibronectin containing the RGD and synergy regions: comparison with the human fibronectin crystal structure. *J. Mol. Biol.*, **277**, 663–682.

Cukierman,E., Pankov,R., Stevens,D.R. and Yamada,K.M. (2001) Taking cell-matrix adhesions to the third dimension. *Science*, **294**, 1708–1712.

Cunningham,B.C. and Wells,J.A. (1993) Comparison of a structural and a functional epitope. *J. Mol. Biol.*, **234**, 554–563.

Du,X., Gu,M., Weisel,J.W., Nagaswami,C., Bennett,J.S., Bowditch,R. and Ginsberg,M.H. (1993) Long range propagation of conformational changes in integrin $\alpha_{IIb}\beta_3$. *J. Biol. Chem.*, **268**, 23087–23092.

Fersht,A.R. (1997) Nucleation mechanisms in protein folding. *Curr. Opin. Struct. Biol.*, **7**, 3–9.

Frank,J., Radermacher,M., Penczek,P., Zhu,J., Li,Y., Ladjadj,M. and Leith,A. (1996) SPIDER and WEB: processing and visualization of images in 3D electron microscopy and related fields. *J. Struct. Biol.*, **116**, 190–199.

George,E.L., Georges-Labouesse,E.N., Patel-King,R.S., Rayburn,H. and Hynes,R.O. (1993) Defects in mesoderm, neural tube and vascular development in mouse embryos lacking fibronectin. *Development*, **119**, 1079–1091.

Goh,K.L., Yang,J.T. and Hynes,R.O. (1997) Mesodermal defects and cranial neural crest apoptosis in alpha5 integrin-null embryos. *Development*, **124**, 4309–4319.

Grant,R.P., Spitzfaden,C., Altroff,H., Campbell,I.D. and Mardon,H.J. (1997) Structural requirements for biological activity of the ninth and tenth FIII domains of human fibronectin. *J. Biol. Chem.*, **272**, 6159–6166.

Hantgan,R.R., Paumi,C., Rocco,M. and Weisel,J.W. (1999) Effects of

ligand-mimetic peptides Arg–Gly–Asp–X (X = Phe, Trp, Ser) on alphaIIbbeta3 integrin conformation and oligomerization. *Biochemistry*, **38**, 14461–14474.

Humphries,J.D., Askari,J.A., Zhang,X.P., Takada,Y., Humphries,M.J. and Mould,A.P. (2000) Molecular basis of ligand recognition by integrin α5β1. II. Specificity of Arg–Gly–Asp binding is determined by Trp157 of the alpha subunit. *J. Biol. Chem.*, **275**, 20337–20345.

Humphries,M.J. (2000) Integrin structure. *Biochem. Soc. Trans*, **28**, 311–339.

Hynes,R.O. (2002) Integrins: bi-directional, allosteric, signalling machines. *Cell*, **110**, 673–687.

Hynes,R.O. and Yamada,K.M. (1982) Fibronectins:multifunctional modular glycoproteins. *J. Cell Biol.*, **95**, 369–377.

Leahy,D.J., Erickson,H.P., Aukhil,I., Joshi,P. and Hendrickson,W.A. (1994) Crystallization of a fragment of human fibronectin: introduction of methionine by site-directed mutagenesis to allow phasing via selenomethionine. *Proteins*, **19**, 48–54.

Leahy,D.J., Aukhil,I. and Erickson,H.P. (1996) 2.0 angstrom crystal structure of a four-domain segment of human fibronectin encompassing the RGD loop and synergy region. *Cell*, **84**, 155–164.

Liddington,R.C. and Ginsberg,M.H. (2002) Integrin activation takes shape. *J. Cell Biol.*, **158**, 833–839.

Mould,A.P., Askari,J.A., Aota,S., Yamada,K.M., Irie,A., Takada,Y., Mardon,H.J. and Humphries,M.J. (1997) Defining the topology of integrin $\alpha_5\beta_1$–fibronectin interactions using inhibitory anti-α_5 and anti-β_1 monoclonal antibodies. *J. Biol. Chem.*, **272**, 17283–17292.

Mould,A.P., Askari,J.A. and Humphries,M.J. (2000) Molecular basis of ligand recognition by integrin $\alpha_5\beta_1$: specificity of ligand binding is determined by amino acid sequences in the second and third NH_2-terminal repeats of the α subunit. *J. Biol. Chem.*, **275**, 20324–20336.

Northrup,S.H. and Erickson,H.P. (1992) Kinetics of protein–protein association explained by Brownian dynamics computer simulation. *Proc. Natl Acad. Sci. USA*, **89**, 3338–3342.

Obara,M., Kang,M.S. and Yamada,K.M. (1988) Site-directed mutagenesis of the cell-binding domain of human fibronectin: separable, synergistic sites mediate adhesive function. *Cell*, **53**, 649–657.

Philippsen,A. (2002) *DINO: Visualizing structural biology*. http://www.dino3d.org

Pierschbacher,M.D. and Ruoslahti,E. (1984) Cell attachment activity of fibronectin can be duplicated by small synthetic fragments of the molecule. *Nature*, **309**, 30–33.

Radermacher,M. (1992) Weighted backprojection methods in electron tomography. In Frank,J. (ed.), *Electron Tomography*. Plenum Press, New York, pp. 91–116.

Radermacher,M., Wagenknecht,T., Verschoor,A. and Frank,J. (1987) Three-dimensional reconstruction from a single-exposure, random conical tilt series applied to the 50S ribosomal subunit of *Escherichia coli*. *J. Microsc.*, **146**, 113–136.

Redick,S.D., Settles,D.L., Briscoe,G. and Erickson,H.P. (2000) Defining fibronectin's cell adhesion synergy site by site-directed mutagenesis. *J. Cell Biol.*, **149**, 521–527.

Shimaoka,M., *et al.* (2003) Structures of the αL I domain and its complex with ICAM-1 reveal a shape-shifting pathway for integrin regulation. *Cell*, **112**, 99–111.

Takagi,J. and Springer,T.A. (2002) Integrin activation and structural rearrangement. *Immunol. Rev.*, **186**, 141–163.

Takagi,J., Erickson,H.P. and Springer,T.A. (2001) C-terminal opening mimics 'inside-out' activation of integrin $\alpha_5\beta_1$. *Nat. Struct. Biol.*, **8**, 412–416.

Takagi,J., Debottis,D.P., Erickson,H.P. and Springer,T.A. (2002a) The role of specificity-determining loop of the integrin β-subunit I-like domain in folding, association with the α subunit and ligand binding. *Biochemistry*, **41**, 4339–4347.

Takagi,J., Petre,B.M., Walz,T. and Springer,T.A. (2002b) Global conformational rearrangements in integrin extracellular domains in outside-in and inside-out signaling. *Cell*, **110**, 599–611.

Weisel,J.W., Nagaswami,C., Vilaire,G. and Bennett,J.S. (1992) Examination of the platelet membrane glycoprotein IIb–IIIa complex and its interaction with fibrinogen and other ligands by electron microscopy. *J. Biol. Chem.*, **267**, 16637–16643.

Wu,L.C., Tuot,D.S., Lyons,D.S., Garcia,K.C. and Davis,M.M. (2002) Two-step binding mechanism for T-cell receptor recognition of peptide MHC. *Nature*, **418**, 552–556.

Xiong,J.P., Stehle,T., Diefenbach,B., Zhang,R., Dunker,R., Scott,D.L., Joachimiak,A., Goodman,S.L. and Arnaout,M.A. (2001) Crystal structure of the extracellular segment of integrin $\alpha_V\beta_3$. *Science*, **294**, 339–345.

Xiong,J.P., Stehle,T., Zhang,R., Joachimiak,A., Frech,M., Goodman,S.L. and Arnaout,M.A. (2002) Crystal structure of the extracellular segment of integrin $\alpha_V\beta_3$ in complex with an Arg–Gly–Asp ligand. *Science*, **296**, 151–155.

Yang,J.T., Rayburn,H. and Hynes,R.O. (1993) Embryonic mesodermal defects in α_5 integrin-deficient mice. *Development*, **119**, 1093–1105.

Received May 8, 2003; revised July 21, 2003; accepted July 22, 2003